Physics of Fluids

Effects of end-walls on flows in a highly loaded compressor cascade with double-circular-arc blades

Cite as: Phys. Fluids **34**, 055124 (2022); https://doi.org/10.1063/5.0091128
Submitted: 11 March 2022 • Accepted: 25 April 2022 • Published Online: 19 May 2022

Yan Jin (金琰), **Changyong Li** (李昌勇), **Juan Du** (杜娟), **et al.**

ARTICLES YOU MAY BE INTERESTED IN

AIP Publishing

Phys. Fluids **34**, 055124 (2022); https://doi.org/10.1063/5.0091128 **34**, 055124

Physics of Fluids ARTICLE scitation.org/journal/phf

Effects of end-walls on flows in a highly loaded compressor cascade with double-circular-arc blades

Cite as: Phys. Fluids **34**, 055124 (2022); doi: 10.1063/5.0091128
Submitted: 11 March 2022 · Accepted: 25 April 2022 ·
Published Online: 19 May 2022

Yan Jin (金琰),[1,a)] Changyong Li (李昌勇),[2] Juan Du (杜娟),[3] and Hongwu Zhang (张宏武)[3]

AFFILIATIONS

[1]Institute of Multiphase Flows, Hamburg University of Technology, 21073 Hamburg, Germany
[2]Center of Applied Space Technology and Microgravity, The University of Bremen, 28359 Bremen, Germany
[3]Institute of Engineering Thermophysics, Chinese Academy of Sciences, 100049 Beijing, China

[a)]Author to whom correspondence should be addressed: yan.jin@tuhh.de

ABSTRACT

A numerical study is carried out to understand the flows in a highly loaded compressor cascade made of double-circular-arc blades, which were measured by Zierke and Deutsch in the late 1980s. A two-dimensional (2D) cascade with periodic boundary conditions in both pitch-wise and span-wise directions and a three-dimensional (3D) cascade with two end-walls that are far away from each other are accounted for in the study. For the incidence angle $\alpha = -8.5^\circ$, the numerical results of the 2D-cascade flow are in excellent accordance with the experimental data. This not only validates the numerical method used in the study but also suggests that a 2D and periodic flow was successfully generated in the experiment for this incidence angle. However, the numerical results of 2D-cascade flows for $\alpha = -1.5^\circ$ and 5° deviate from the experiment considerably because the strong effects of the end-walls on the wake are neglected in the simulation. By contrast, the simulation of 3D-cascade flows predicts an accurate pressure coefficient at the blade surface, the pressure increase coefficient, and the total pressure loss coefficient for all three incidence angles. This means that, to generate experimental data for validating numerical simulation, it is important to consider the effect of end-walls when the incidence angle is large. The numerical results also show that, for 2D-cascade flows with a low inlet turbulence intensity, the laminar-turbulent transition on the pressure surface is determined by the interaction of the Klebanoff distortions and T-S waves. The Klebanoff distortions are also clearly identified on the suction surface for $\alpha = -8.5^\circ$. The end-walls induce span-wise elongated disturbances, which suppress the stream-wise disturbances. The transition in 3D-cascade flows generally follows the mechanism of natural transition.

I. INTRODUCTION

Design of gas turbines with high efficiency is significant in modern industry. Highly loaded blade cascades are often adopted in modern gas turbines to reduce their weight. However, they often lead to complicated turbulent flows, resulting in serious irreversible losses. Understanding the turbulent flows in highly loaded compressor cascades is essential for the design of modern gas turbines.

A famous experimental study of highly loaded compressor cascades was carried out by Zierke and Deutsch in the late 1980s. They made extensive measurements of flows in a double-arc compressor blade cascade. An interesting phenomenon is that, although profound experimental data were published by Zierke and Deutsch,[1–5] very few numerical studies used these data to validate their solvers and turbulence models. The numerical studies about this highly loaded compressor cascade are listed in Table I. An evident deficiency of these numerical studies is that, while the inlet turbulence intensity in the experiment was 0.18%, the numerical studies used much higher values to avoid the calculation of transition.

A possible reason for this phenomenon (a lack of numerical studies) is that, "the boundary layer on the suction surface was dominated by a separation bubble in the absence of wakes or high free-stream turbulence," see comments by Cumpsty and Dong at the end of Zierke and Deutsch.[5] It is difficult to simulate the effect of this bubble on the laminar-turbulent transition. In the answers to these comments, Zierke and Deutsch also stated that "the transition process on turbomachinery blades will be extremely difficult to model."

The purpose of this study is to better understand the turbulent flows in the highly loaded compressor cascade measured by Zierke

TABLE I. Numerical studies of the flows in a double-arc compressor blade cascade.[5]

References	Turbulence model	Inlet turbulence intensity
Vlahostergios[6]	RANS: SA; (SST) $k-\omega$ BSL-RSM SSG-RSM	22%
Du *et al.*[7]	RANS: SST $k-\omega$	3%

and Deutsch, including the bubble separation near the leading edge, laminar-turbulent transition, passage vortex, wake, etc. For this purpose, we have carried out a high-accuracy numerical study.

The selection of an appropriate turbulence model is a prerequisite of this study. Reynolds-averaged Navier–Stokes simulation (RANS) is the most popular method for simulating cascade flows, see Refs. 6–9 as examples. However, RANS solutions sometimes have considerable uncertainties. Jin and Herwig[10] calculated the turbulent flows in a rough wall channel using different RANS models, including $k-\varepsilon$, $k-\omega$, and Reynolds stress (RSM) models. The numerical results show that the errors of all these RANS models are higher than 20%. Moreover, for the compressor cascade flows under consideration, an additional transition model has to be added to simulate the laminar-turbulent transition, this leads to new uncertainties of the numerical solution.

Direct numerical simulation (DNS) is the most accurate simulation method for fundamental studies of turbulent flows; however, it requires extremely high computational costs. Due to this reason, the DNS is more often used to simulate the flows in two-dimensional (2D) compressor cascades and with a reduced Reynolds number, see Refs. 11 and 12 as examples. Large eddy simulation (LES) requires a lower computational cost; however, simulation of compressor cascade flows is still very expensive, due to the high Reynolds numbers based on the chord length and free stream velocity.[13–19] The computational costs for typical LES studies of flows in three-dimensional (3D) compressor cascades are shown in Table II. It might be seen that the grid points for a typical LES is on the order of 10^8, while the CPU time is on the order of 10^6 h. In general, with the current computing power, LES is still only suitable for calculating a few typical cases rather than a massive parametric study.

TABLE II. Computational costs for typical LES studies of compressor cascade flows.

References	Re ($\times 10^6$)	Span-wise extent	Grid points ($\times 10^6$)	CPU processors	CPU h ($\times 10^6$)
Gao *et al.*[13]	0.38	0.5	200	856	2000
Scillitoe *et al.*[14]	0.23	0.65	69	960	161
Min *et al.*[15]	0.38	0.5	600	64 000	1536
Li *et al.*[16]	0.45	1	130	10 000	2000
Li *et al.*[17]	0.1	0.5	120	528	350
Zhu *et al.*[18]	0.38	0.5	15	⋯	⋯
This study	0.5	1	16	28	6
	0.5	1	50	384	80

Some other methods, such as delayed detached eddy simulation (DDES)[20–22] and detached eddy simulation approach (DES),[23–25] cannot capture laminar-turbulent transition without introducing a transition model. In addition, to our point of view, they introduce too strong artificial dissipation near the wall; however, the accurate calculation of the motions in the near-wall region is important for understanding the irreversible losses in compressor cascades.

Jin[26] interpreted the turbulence modeling in a different way and proposed a new method, the parameter extension simulation (PES) method, for simulating turbulent flows. It is composed of a modified mixing length (ML+) model for calculating the reference solution and a parameter extension method for correcting the solution. This method was used to simulate the flows in a regular compressor cascade made of airfoils NACA0065-009[26,27] and compared with the experiments by Ma[28] and Zambonini *et al.*[29] It was found that, without a parameter extension, the reference solution is already as accurate as a traditional LES solution. The laminar-turbulent transition was also precisely captured in the numerical results. However, it only used 16×10^6 mesh cells to calculate the whole span, while a traditional LES[13] used 200×10^6 grid points for only a half-span. A much lower computational cost is needed by the new turbulence model, making it particularly suitable for the current study because intensive numerical simulations need to be carried out to find the appropriate boundary conditions in the span-wise direction. This turbulence model will be introduced in Sec. II and used in the study. The description of test cases, numerical results, and conclusions are given in Secs. III, IV, and V, respectively.

II. PROBLEM STATEMENT, MATHEMATICAL MODEL, AND NUMERICAL METHODS

A. Statement of problem

Flows in a highly loaded compressor cascade made of double-circular-arc blades, which were measured by Zierke and Deutsch,[1–5] are simulated numerically. Table III summarizes the blade geometry. The camber angle ϕ, which is the difference between the inlet and outlet blade metal angles $\kappa_1-\kappa_2$, for this highly loaded cascade is 65°. This camber angle is much higher than that of a regular compressor. For example, the regular compressor cascade made of airfoils NACA0065-009[27] has the camber angle of 23.2°. A larger camber angle results in a larger fluid turning angle and, thus, a higher loading.

TABLE III. Geometric parameters of the highly loaded blade-profile.

Parameters	Values
Chord (m)	0.229
Camber angle ϕ (°)	65
Stagger angle γ (°)	20.5
Pitch spacing s (m)	0.107
Solidity σ	2.14
Aspect ratio AR	1.61
Inlet blade metal angle κ_1 (°)	53
Outlet blade metal angle κ_2 (°)	−12

In the experiment, Zierke and Deutsch tried to create a periodic and 2D flow by employing a strong suction, which was controllable in the blade-to-blade direction, just upstream of the blade leading edge line. In our numerical simulation, we have created a periodic and 2D flow near the mid-span by using two methods. In the first method, periodic boundary conditions are given in both pitch-wise and span-wise directions. The stream-wise–pitch-wise ($x_1 - x_2$) section of the computational domain is shown in Fig. 1.

A periodic boundary condition is only given in the pitch-wise direction in the second method. Two end-walls are added in the span-wise directions, so the cascade is 3D. A statistically periodic and 2D flow can be obtained near the mid-span when the span is long enough. Hereby, similar to the experiments by Ma[28] and Zambonini,[29] the span width is set to be 0.37 m.

B. Mathematical equations

The cascade flow under consideration can be treated as an incompressible flow because of the low Mach number. The governing equations of a generic turbulence model are as follows:

$$\frac{\partial u_i}{\partial x_i} = 0, \tag{1}$$

$$\frac{\partial u_i}{\partial t} + \frac{\partial (u_i u_j)}{\partial x_j} = -\frac{\partial p}{\partial x_i} + \nu \frac{\partial^2 u_i}{\partial x_j^2} + g_i + \mathcal{M}_i. \tag{2}$$

$\mathcal{M}_i$ is a generic modeling term, which can be the modeled Reynolds stress term for RANS or the SGS term for LES.

Jin[26] interpreted the turbulence model differently from RANS and LES. According to this interpretation, a turbulence model introduces an artificial dissipation, which dissipates small eddies. The calculation can be performed with a lower mesh resolution (compared with DNS), when small eddies are dissipated. Thus, the purpose of turbulence modeling is to dissipate more small eddies without changing the statistical solution qualitatively. It is expected more small eddies can be dissipated where the turbulence is stronger. Thus, the length scale used in a turbulence model should be the characteristic length of turbulence.

Based on the interpretation described above and the classic mixing length (ML) model, Jin[26] developed a modified mixing length model for calculating the turbulent flows. The corresponding simulation is a special LES, in which the small eddies are dissipated instead of modeled. Thus, this turbulence model is also called a small-eddy-dissipation mixing length (SED-ML) model. It was used to calculate the reference solution for a parameter extension simulation (PES). Nevertheless, it was found that the reference solution (without a parameter extension) is already as accurate as classic LES, while it requires a much lower computational cost. This characteristic is particularly suitable to this research because intensive simulations need to be carried out to find the appropriate boundary conditions in the span-wise direction. Therefore, we use the SED-ML model (without a parameter extension) in our numerical study.

$\mathcal{M}_i$ in the SED-ML model is modeled as the product of a dissipation strength indicator ϕ and a dissipative force distribution F_i, i.e., $\mathcal{M}_i = \phi F_i$. F_i is proposed based on the eddy viscosity assumption, expressed as

$$F_i = \frac{\partial}{\partial x_j}\left(\nu_{eff} \frac{\partial u_i}{\partial x_j}\right), \tag{3}$$

where ν_{eff} is an effective viscosity. We can use a modified mixing length l'_{mix} to approximate the turbulence length scale and $\vartheta_{mix} = l'_{mix}|s_{ij}|$ as the characteristic velocity, where $|s_{ij}| = (2 s_{ij} s_{ij})^{1/2}$ is the magnitude of the transient strain rate s_{ij}. Then, the effective viscosity ν_{eff} in Eq. (3) is calculated as

$$\nu_{eff} = l'^2_{mix}|s_{ij}|. \tag{4}$$

To propose l'_{mix}, we introduce the following local transient length scale,

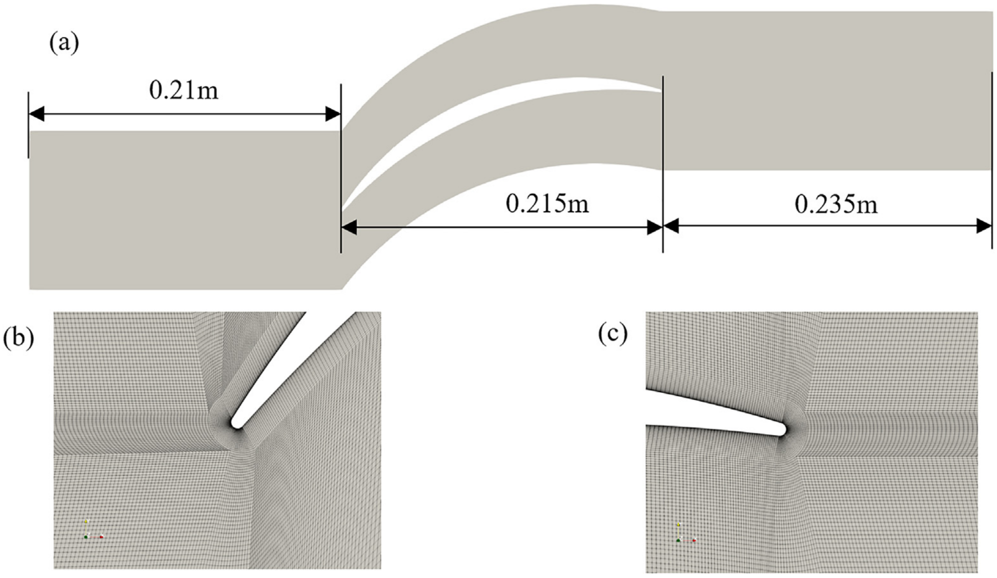

FIG 1. Computational domain (a) and meshes near the blade leading edge (b) and trailing edge (c).

$$l_l = \sqrt{\frac{|\partial K/\partial t|}{|s_{ij}|^3}}, \quad l_s = \sqrt{\frac{\nu}{|s_{ij}|}}, \tag{5}$$

where $K = \frac{1}{2}u_k^2$ is the instantaneous kinetic energy, l_l characterizes the length scale of transient velocity fluctuation , l_s characterizes the viscous length scale, which is identical to the classic viscous length scale $\frac{\nu}{u_\tau}$ at the wall. Both l_l and l_s can be calculated from the transient flow field directly, without using any statistical results. Using l_l, and l_s, we can establish the following local transient dimensionless number,

$$y_s^+ = \frac{l_l}{l_s} = \sqrt{\frac{|\partial K/\partial t|}{\nu|s_{ij}|^2}}. \tag{6}$$

Similar to the classic mixing length, l'_{mix} is calculated as

$$l'_{mix} = \kappa y_w F_1\left(y_s^+\right). \tag{7}$$

$F_1\left(y_s^+\right)$ damps the mixing length near the wall, expressed as

$$F_1\left(y_s^+\right) = 1 - \exp\left(-y_s^+/A^+\right). \tag{8}$$

$A^+ = 1$ is a model constant. It can be seen that calculation of the friction velocity u_τ in the damping function proposed by Driest[30] has been avoided in the damping function (8). $F_1\left(y_s^+\right)$ becomes zero not only at the wall but also when the flow is steady, so the model is also valid for steady flows.

ϕ acts as a small perturbation parameter in the turbulence model. The small-eddies that are dissipated by the modeling term $\mathcal{M}_i$ can be controlled by adjusting the value of ϕ. We set its default value ϕ_0 to 0.004. It yields accurate solutions for all test cases in our benchmark study, including smooth/rough wall channel flows and compressor cascade flows, see Refs. 26 and 27.

C. Numerical method

For the simulations, a finite volume-method (FVM) was utilized. The solver was developed based on our DNS solver by using the open source code package OpenFoam. The DNS solver has received intensive validations in the previous DNS studies.[31–35] The spatial discretization was implemented by a second-order central-difference scheme. For time derivatives, the second-order implicit backward method was used. For the correction and coupling of the pressure and velocity fields, the pressure-implicit scheme with splitting of operators (PISO) algorithm was used.[36] A stabilized preconditioned (bi-)conjugate gradient solver was utilized to solve the pressure field and the momentum and species concentration equations.

III. DESCRIPTION OF TEST CASES

Flows of three incidence angles, $\alpha = -8.5°$, $-1.5°$, and 5°, are simulated in this study. A divergence free synthetic eddy method[37] is used to approximate inlet velocity fluctuations. For the two-dimensional cascade, the turbulence intensity is set to 0.18%, which is the same as the value in the experiment. For the three-dimensional cascade, because there is a lack of information in the experiment, the end-walls is established artificially. The span-width of the regular compressor cascade tested by Ma,[28] which is 0.37 m, is used in the study. The velocity profile in Ma[28] is adjusted by multiplying a factor to fit the free stream velocity and turbulence intensity.

The details about the flow conditions and the computational meshes are shown in Table IV. Two meshes are used for both 2D-cascade and 3D-cascade flows. Their distributions near the leading and trailing edges are shown in Figs. 1(b) and 1(c), respectively. The distance from the first mesh cell to the blade surface in wall units Δy_w^+ is generally smaller than 1, except a few cells near the leading and trailing edges. The results of lower mesh resolutions are used in the analysis, while typical test cases are calculated with a higher mesh resolution to perform the mesh-convergence study, which is introduced in Appendixes A and B in detail. Using a similar mesh resolution as mesh C, the flows in a regular 3D-cascade have been calculated using the same solver, see Ref. 26. The pressure coefficients and total pressure loss coefficients at different span sections have been carefully validated with the experimental data. This validates the numerical results in this study indirectly.

A flow for about 0.04 s needs to be calculated to obtain the statistically converged results, while a calculation for another 0.04 s is needed to calculate the statistical results. The computational time and resources for a typical test case are shown in Table II. It can be seen that, when the number of mesh cells is increased by 3×, the required computational time is increased by about 12×.

IV. RESULTS AND DISCUSSION

A. 2D-cascade flows

Our numerical study is started with the flows in the 2D-cascade. Figure 2 shows the instantaneous velocity component u_3 near the

TABLE IV. Test cases used in the study. Meshes A and C: 16 × 10^6 mesh cells with 128 cells in the span-wise direction; Meshes B and D: 50 × 10^6 mesh cells with 200 cells in the span-wise direction.

Cascade	Incidence angle α	Inlet velocity u_{inl} (ms^{-1})	Mesh	Δy_w^+	$\overline{\Delta t}$ (s)
2D-cascade (without end-walls)	$-8.5°$	33.28	A	0.4–5.3	6.6×10^{-7}
	$-1.5°$	32.88	A	0.2–5.5	7.4×10^{-7}
	5°	33.11	A	0.2–5.9	6.5×10^{-7}
			B	0.1–3.7	4.6×10^{-7}
3D-cascade (with end-walls)	$-8.5°$	33.28	C	0.3–5.4	6.8×10^{-7}
	$-1.5°$	32.88	C	0.1–5.5	7.6×10^{-7}
	5°	33.11	C	0.1–5.9	6.7×10^{-7}
			D	0.1–3.9	6.4×10^{-7}

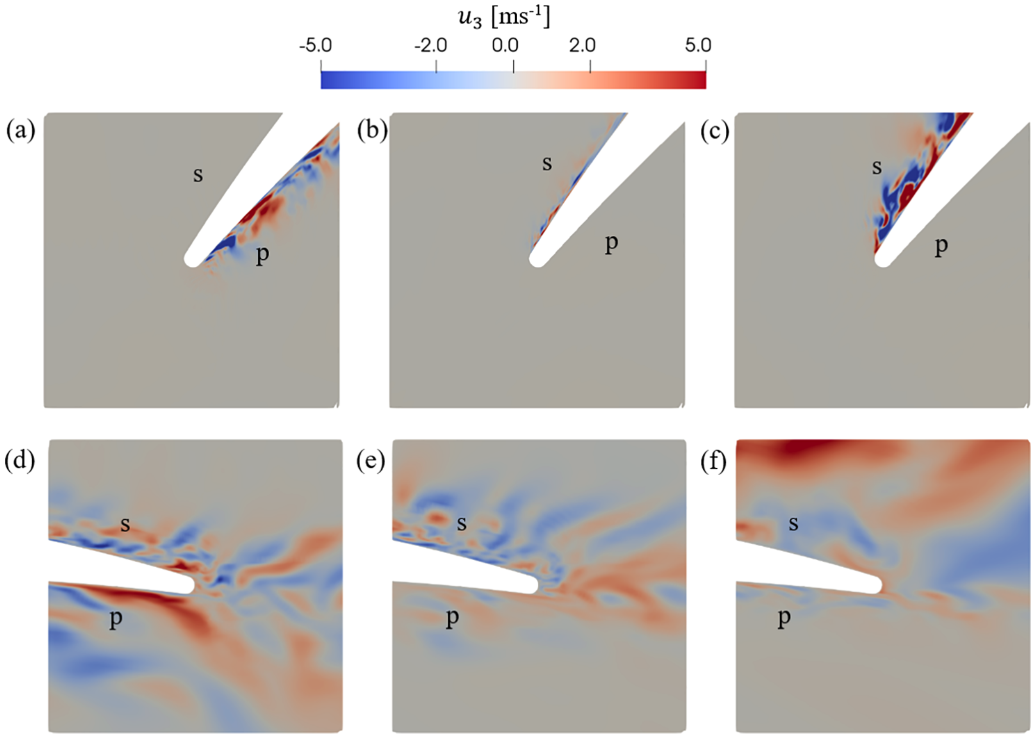

FIG 2. Instantaneous velocity component in the span-wise direction u_3 near the blade leading edge (a–c) and trailing edge (d–f), 2D-cascade flows (without end-walls). The incidence angles are $\alpha = -8.5°$ (a, d), 1.5° (b, e), and 5° (c, f).

leading edge and trailing edge. For $\alpha = -8.5°$, a separation bubble, which leads to an immediate transition and instability, can be found near the leading edge of the pressure surface [Fig. 2(a)]. The separation bubble near the pressure surface leading edge disappears when the incidence angle is increased to $-1.5°$, while another tiny separation bubble originates near the suction surface [Fig. 2(b)]. The instability induced by the separation bubble is considerably enhanced when the incidence angle is further increased to 5°. Significant flow separations can be found near the trailing edge for all incidence angles. With an increase in the incidence angle, the vortices become larger and move more slowly, leading to the low-frequency oscillations.

The flow phenomena described above were also remarked in the experimental study by Zierke and Deutsch. However, as shown in Fig. 3, while the numerical results of the pressure coefficient C_p for $\alpha = -8.5°$ are in good accordance with the experimental data, the numerical simulation predicts much higher C_p than experiments for large incidences angles ($\alpha = -1.5°$ and 5°). Hereby, C_p is defined as

$$C_p = \frac{\overline{p} - p_{inl}}{1/2\, u_{inl}^2}, \tag{9}$$

where p_{inl} is the mean static pressure at the mid-plane of the inlet. The operator $^-$ denotes time-averaging. c_a in Figure 3 is the span width in the axial direction.

The gap between the numerical simulation and experiment becomes larger with an increase in the incidence angle. Calculated C_p is not closer to the experiment when a higher mesh resolution is used, see Appendix A. This trend is very similar to what was found in the LES study of flows in a regular compressor cascade,[38] which shows that the pressure coefficient C_p is over-predicted if the effects of end-walls are not accounted for. The possible reason is that the end-walls result in rolling-up of the flow and thus lead to more loss of the kinetic energy near the mid-span. Although the statistical results near the mid-span are 2D and periodic, the transient flow field is still affected by the end walls. The loss caused by the end-walls is not accounted for in the 2D-cascade flows, so the pressure increase $p_{out} - p_{inl}$ is over-predicted. Considering the outlet pressure p_{out} is set to a constant, the reference pressure p_{inl} in Eq. (9) is under-predicted. Therefore, the profiles for the pressure coefficient are shifted upward. This hypothesis will be further validated in the next sections.

B. 3D-cascade flows

Similar to the numerical results by Jin,[26] C_p becomes lower when the end-walls are accounted for, see Fig. 4. For $\alpha = -8.5°$, the profiles of c_p are slightly shifted downwards by the end-walls. Zierke and Deutsch[5] employed a strong suction in the experiment, just upstream of the blade leading edge. The suction weakens the effect of end-walls, making the cascade flow for $\alpha = -8.5°$ close to a 2D and periodic flow. This suction is not accounted for in the 3D-cascade simulation, while the end-walls still have some effects on the flow near the mid-span. This explains why the numerical results of 2D-cascade flows are closer to experiments than those of 3D-cascade flows at $\alpha = -8.5°$.

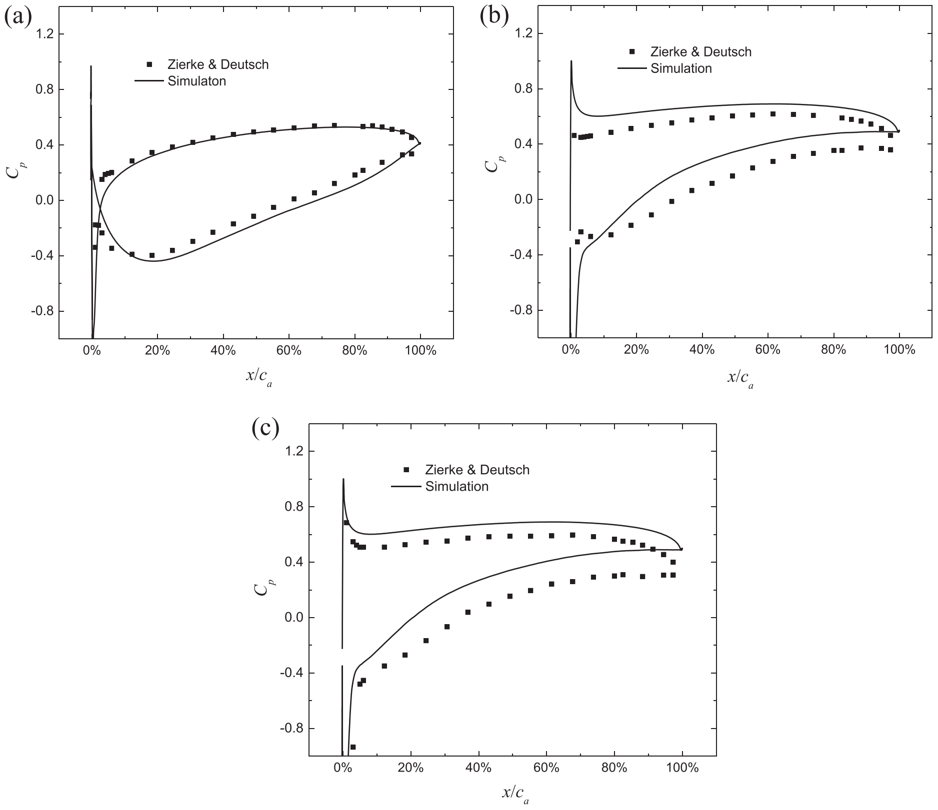

FIG 3. Pressure coefficient at the airfoil surface for 2D-cascade flows. A periodic boundary condition is used in the spanwise direction. (a) $\alpha = -8.5°$, (b) $\alpha = -1.5°$, and (c) $\alpha = 5°$.

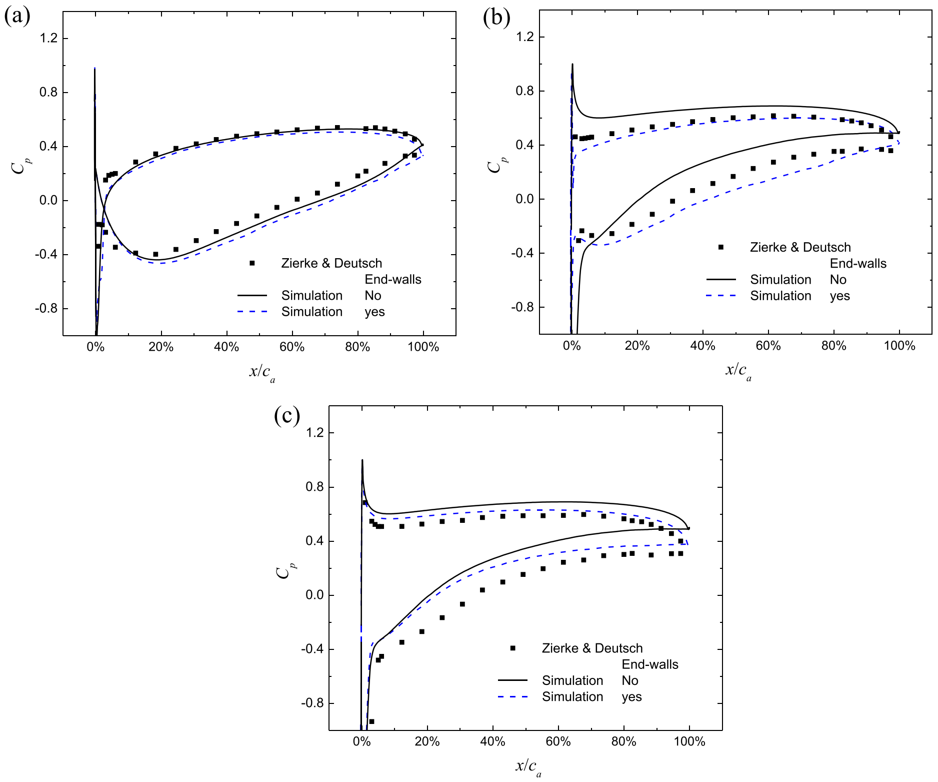

FIG 4. Pressure coefficient C_p at the airfoil surface of the mid-span for $\alpha = -8.5°$ (a), $\alpha = -1.5°$ (b), and $\alpha = 5°$ (c).

However, the discrepancy between the experiment and simulations (with and without end-walls) is marginal. This means that the effect of end-walls for $\alpha = -8.5°$ can be neglected.

For larger incidence angles ($\alpha = -1.5°$ and 5°), calculated C_p is much closer to the experimental data when the effects of end-walls are considered. A possible reason is that the end-walls stimulate strong rolling-up of flows at a large incidence angle; however, no special treatments were adopted in the experiment to eliminate the wall effects in the wake. The rolling-up of flows might result in more losses of the kinetic energy near the mid-span, and thus lead to a lower pressure rise. This can be validated by comparing the numerical and experimental results for the pressure increase coefficient C_{p2} and total pressure loss coefficient ω at the mid-span 31.9% downstream of the blade trailing edge, see Figs. 5 and 6. C_{p2} and ω are defined as

$$C_{p2} = \frac{p_{out} - p_{inl}}{1/2\, u_{inl}^2}, \tag{10}$$

$$\omega = \frac{p_{T,inl} - \bar{p}_{T,out}}{1/2\, u_{inl}^2}, \tag{11}$$

where the subscript "out" denotes a plane downstream of the blade trailing edge.

Figure 5 shows that, without end-walls, the pressure increase coefficients C_{p2} for $\alpha = -1.5°$ and 5° are over-predicted. This may explain why C_p at the airfoil surfaces for these incidence angles are shifted upwards, see Fig. 3. In addition, the total pressure loss coefficient ω has the lowest value at $\alpha = -1.5°$, and this is also different from the experimental data, see Fig. 6. By contrast, when the effects of end-walls are considered, the numerical results for c_p and ω are much closer to the experimental data.

C. Flows over pressure surface

Figure 7 shows the vortices identified by the iso-surfaces of the second invariant of the instantaneous velocity gradient tensor Q, defined as $-\frac{1}{2}\frac{\partial u_i}{\partial x_j}\frac{\partial u_j}{\partial x_i}$. The numerical results of both 2D- and 3D-cascade flows indicate that the flows are fully turbulent over almost the whole pressure surface. However, vortical tubes elongated in the span-wise direction dominate the flow near the mid-span when the end-walls are considered. Without end-walls, however, stream-wise elongated vortices play a more important role.

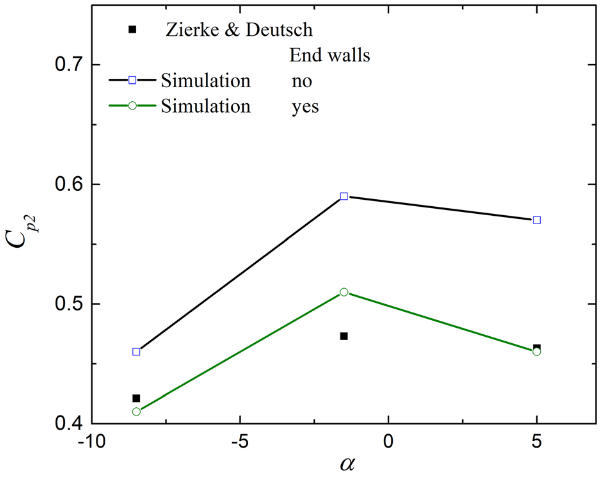

FIG 5. Pressure increase coefficient C_{p2} at the plane $0.319c_a$ downstream of the airfoil trailing edge.

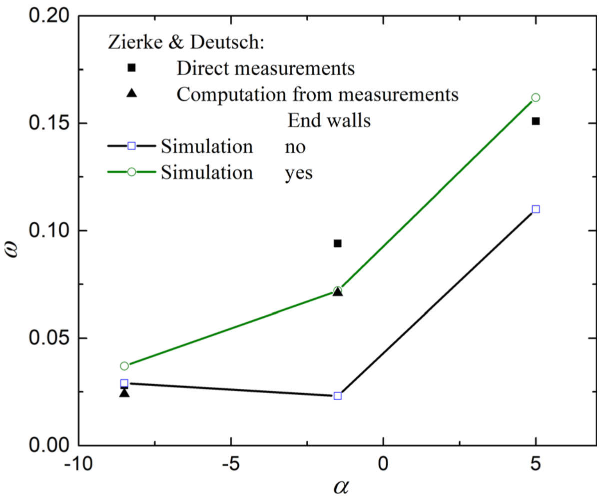

FIG 6. Total pressure loss coefficient ω at the plane $0.319c_a$ downstream of the airfoil trailing edge.

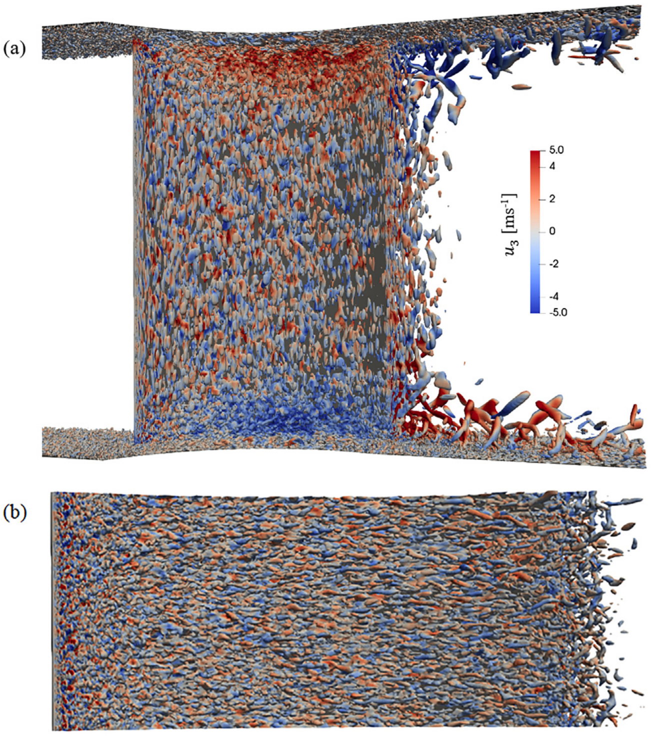

FIG 7. Iso-surfaces of $Qc^2/u_m^2 = 50$ colored with the velocity component in the spanwise direction u_3 over the pressure surfaces for the 3D-cascade flow (a) and 2D-cascade cascade flow (b), $\alpha = -8.5°$.

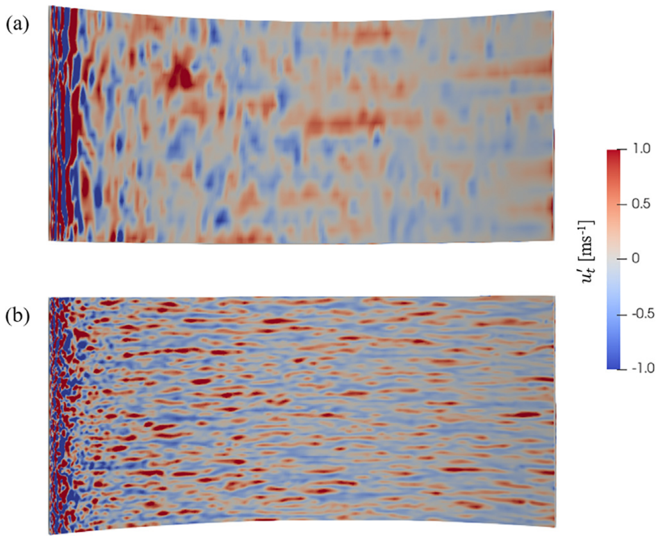

FIG 8. Contours of the instantaneous tangential velocity perturbation u_t' near the mid-span for $\alpha = -8.5°$. Results of the 3D-cascade flow (a) are compared with those of the 2D-cascade flow (b).

These features are confirmed by the contours of the instantaneous tangential velocity perturbations u_t' in a layer, which is 1.5×10^{-5} m away from the airfoil surface, see Fig. 8. The layer is within the viscous sublayer ($y_w^+ \leq 5$). For the 3D-cascade flow, the flow field close to the mid-span with the same span width as the 2D-cascade is shown [Figure 8(a)] to make the comparison.

Both 2D- and 3D cascade flows show that span-wise elongated vortices originate near the leading edge of the airfoil. They represent the separation bubble observed in the experiment. The friction coefficient C_f at the pressure surface reaches a local minimal value where the separation bubble originates, see Fig. 9(a). Then, C_f rises downstream of the separation bubble, suggesting the transition to turbulence and recovery of the boundary layer. Without end-walls, the spanwise elongated vortical tubes break into to three-dimensional vortices, due to the instabilities in the stream-wise direction. With end-walls; however, the span-wise elongated instabilities are sustained and enhanced.

Numerical simulations suggest that the transition is completed at about $0.5\%c_a$, indicated by a peak value of C_f. The end-walls do not have a significant influence on the location of transition. However, the maximum value of C_f is considerably reduced by the end-walls. C_f drops again from $0.5\%x_a$, suggesting the occurrence of flow

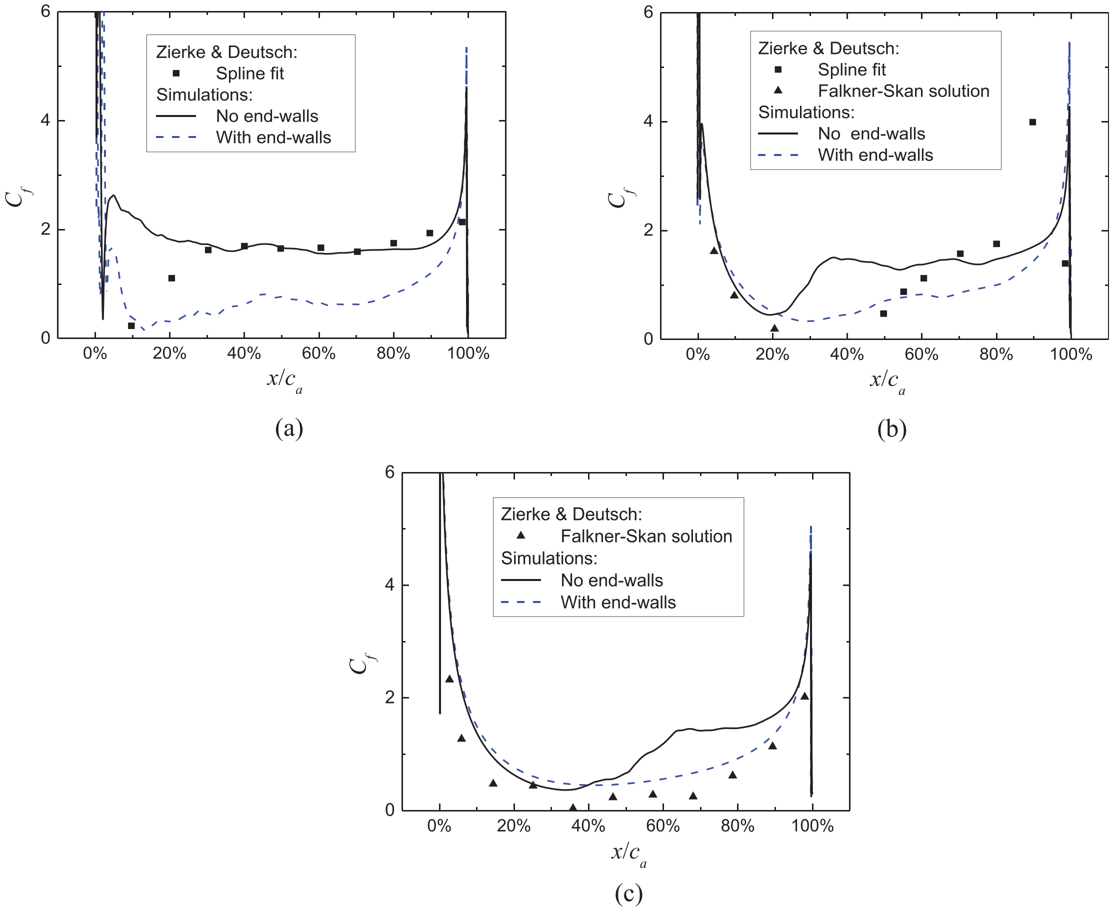

FIG 9. Friction coefficient over the pressure surface for $\alpha = -8.5°$ (a), $-1.5°$ (b), and 5° (c).

separations. Without end-walls, stream-wise elongated disturbances are clearly identified in the zone of flow separations, see Figure 8(b). These stream-wise perturbations are considerably weakened by the end-walls, while they induce span-wise elongated disturbances, see Figure 8(a). The stream-wise perturbations can be found close to the blade trailing edge for both 2D- and 3D-cascade flows, due to the favorable pressure gradient in this region, see Figure 4(a).

The numerical results for C_f are compared with the experimental data of Zierke and Deutsch that were processed with a spline fit or the solutions of Falkner and Skan.[39] More details about these processing methods can be referred to Refs. 1–5. A slow transition in a long distance is observed in the experiment, identified by the increase in C_f from 10%c_a to 30%c_a. It is expected that the suction employed in the experiment slows down the transition; however, its effect cannot be modeled in the simulation. Despite this gap, the results of C_f for the 2D-cascade flow are in good accordance with the experiment, in particular in the region where the turbulence is fully developed ($x \geq 30\%c_a$). With end-walls, the predicted C_f is lower than the experiment because the end-walls induce span-wise elongated vortices and enhance the flow separation. The numerical results of the 3D-cascade flow show that, although the mean inlet and outlet velocity profiles are 2D and periodic near the mid-span, the end-walls still have significant effects on the transient flow in this region.

For $\alpha = -1.5°$, the numerical results still indicate a local minimum value of C_f close the leading edge, see Figure 9(b). It corresponds to a small separation bubble, which can be also found in the contours of u_t', see Figure 10. This separation bubble nevertheless has not transited to turbulence. The transition starts at 20%x_a for the 2D-cascade flow and at 30%c_a for the 3D-cascade flow, indicated by an increase in C_f from its local minimum value. This is in accordance with the statement by Zierke and Deutsch that the transition occurs between 3%c_a and 62%c_a. However, the experiment shows that C_f still increases sharply from 50%c_a to 70%c_a, suggesting that the transition is not completed upstream of 70%c_a. The simulations predict that the transition is completed at 38%c_a for the 2D-cascade flow and at 52%c_a for the 3D-cascade flow. This is consistent with our discussions above that the suction employed in the experiment slows down the transition.

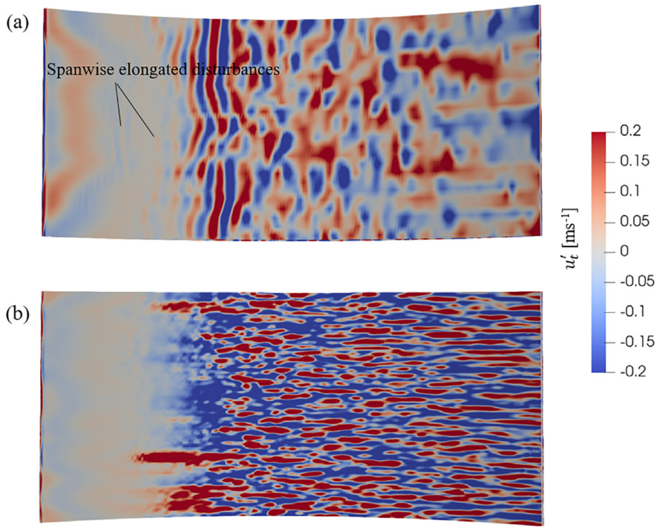

FIG 10. Contours of the instantaneous tangential velocity perturbation u_t' near the mid-span for $\alpha = -1.5°$. Results of the 3D-cascade flow (a) are compared with those of the 2D-cascade flow (b).

Figure 10 shows the distinctly different mechanisms of transition for 2D- and 3D-cascade flows. When the end-walls are considered, span-wise waves can be clearly seen in Figure 10(a) upstream of where the transition starts (at about 30%c_a). These waves are close to the Tollmien–Schlichting (T–S) waves; however, they are not completely 2D. Thereafter, the waves become 3D, and the flow becomes fully turbulent. This is a typical characteristic of natural transition.

Without end-walls, see Figure 10(b), we can still observe the nearly two-dimensional T–S waves upstream of the starting point of transition (at about 20%x_a). These waves are nevertheless affected by the streamwise elongated disturbances. After the flow becomes fully turbulent, stream-wise elongated disturbances still dominate the flow within the viscous sub-layer. This is also different from the 3D-cascade flow, which shows strong span-wise perturbations.

The separation bubble near the leading edge of the pressure surface can still be found at $\alpha = 5°$. It is identified by a local minimum value of C_f and leads to the disturbances stretched in the span-wise direction, see Figure 11. This separation bubble for the 2D-cascade flow can be also visualized by the iso-surfaces of Q in Figure 11(c).

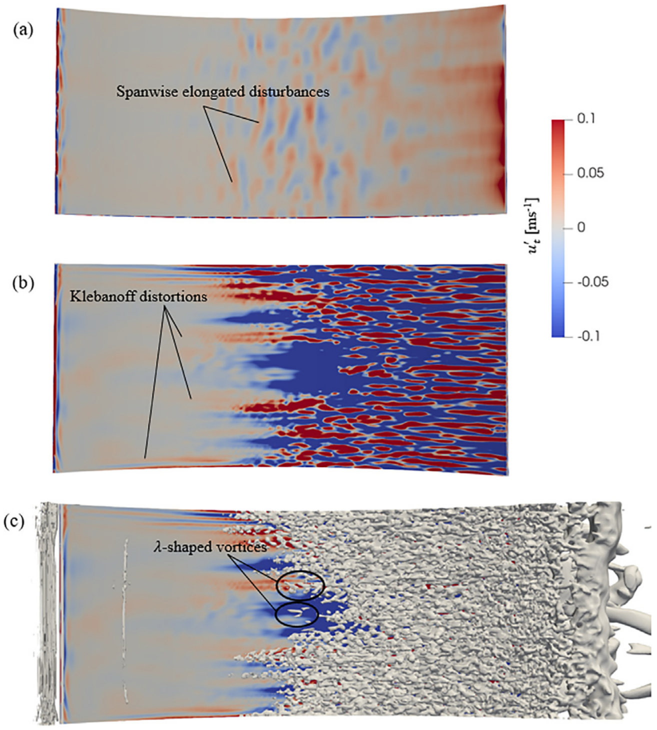

FIG. 11. Contours of the instantaneous tangential velocity perturbation u_t' over the pressure surface near the mid-span for $\alpha = 5°$. Results of the 3D-cascade flow (a) are compared with those of the 2D-cascade flow (b and c). The vortices identified by iso-surfaces of Q are shown in (c).

Similar to the flow for $\alpha = -1.5°$, the separation bubble does not result in transition. The transition starts at 37%c_a in the 2D-cascade flow, while it starts at 42%c_a in the 3D-cascade flow. The experiment by Zierke and Deutsch suggested that the boundary layer begins to transit at 35.1%c_a, which is close to the numerical solution. However, while the simulation of the 3D-cascade flow and the experiment show that the transition is not completed, the simulation of the 2D-cascade flow suggests that the transition is completed at 65%c_a, downstream of which the flow separation occurs.

The transition of the 3D-cascade flow still generally follows the mechanism of natural transition in which 2D T–S waves evolves into 3D instabilities. For the 2D-cascade flow, the Klebanoff distortions, which are the stream-wise elongated disturbances, can be found upstream of the starting point of transition, see Figure 11(b). Bypass transition, in which stream-wise-elongated disturbances are forced by the low-frequency component of free-stream turbulence, does not occur because of the low free-stream turbulence intensity in this study. By contrast, Figure 11(c) shows that the 3D instabilities originate from the viscous sublayer. Some λ-shaped vortices are also identified by the iso-surfaces of Q. These are the characteristics of the secondary instability of natural transition in which spanwise-periodic λ-patterns develop on the top of the T–S waves. Figure 12 shows the iso-surfaces of the instantaneous normal velocity perturbation u'_n in which the λ-shaped vortices are identified by the positive streaks of u'_n. The numerical results show that the transition is determined by the interaction between the Klebanoff distortions and the T–S waves. This is in accordance with the DNS study by Zaki.[11]

D. Flows over suction surface

Figure 13 shows the vortices over the suction surface for $\alpha = -8.5°$, identified with the iso-surfaces of Q. For the 3D-cascade flow, the span-wise vortical tubes start to appear at 42%c_a near the mid-span. This location corresponds to a local minimum value of C_f, see Figure 14(a), which indicates where the transition starts.

Figure 15 shows the instantaneous tangential velocity perturbations u'_t at the surface 1.5×10^{-5} m above the suction surface, which is in the viscous layer. It can be seen in Figure 15(a) that the flow is laminar upstream of 40%c_a for the 3D-cascade flow. Streaks in the spanwise direction, which are disturbed in the stream-wise direction, can be found where the transition takes place. They correspond to the vortical tubes elongated in the span-wise direction in Figure 13(a). C_f reaches a peak value at 52%c_a, suggesting that the transition is completed and the flow starts to separate. The span-wise elongated vortical tubes break into three-dimensional vortical structures from this location; however, they are still strongly stretched in the span-wise direction.

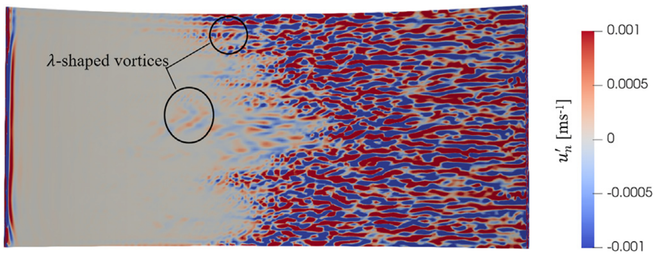

FIG. 12. Contours of the instantaneous normal velocity perturbation u'_n over the pressure surface near the mid-span for $\alpha = 5°$. Results of the 2D-cascade flow are shown.

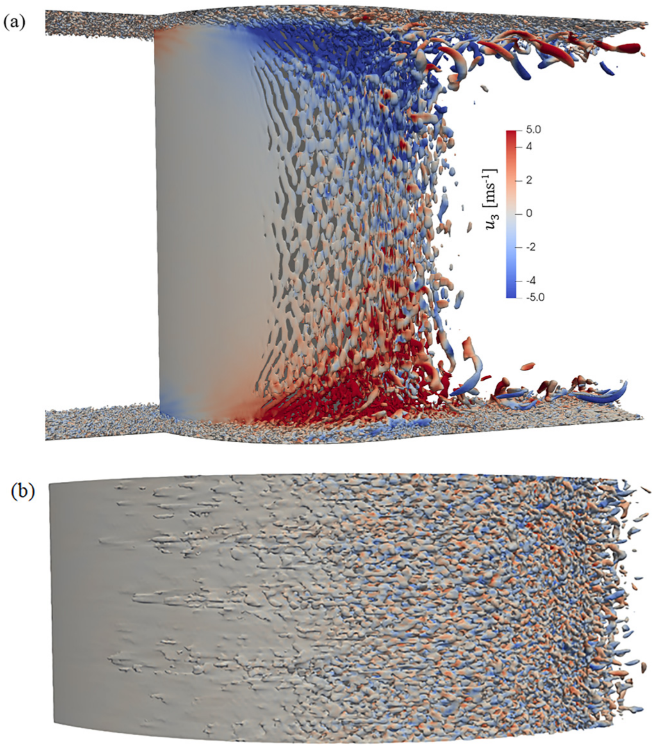

FIG 13. Iso-surfaces of $Qc^2/u_m^2 = 50$ colored with the velocity component in the spanwise direction u_3 over the suction surfaces for the 3D-cascade flow (a) and 2D-cascade flow (b), $\alpha = -8.5°$.

The iso-surfaces of Q for the 2D-cascade flow suggest much weaker perturbations in the span-wise direction, see Figure 13(b). The local minimum value of C_f shows that the transition takes place at 41%c_a, which is close to the result of the 3D-cascade flow. The transition is completed at 60%c_a, indicated by the peak value of C_f. A flow separation occurs after the flow becomes fully turbulent. The experiment by Zierke and Deutsch indicated that transition is completed at 70%c_a, which is mildly later than the numerical results. Despite this gap, the numerical results of the 2D-cascade flow are in good accordance with the experiment.

For $\alpha = -1.5°$, C_f has a local minimal value near the blade leading edge in both 2D- and 3D-cascade flows, indicating the existence of a separation bubble. This is in accordance with the experimental observations. The boundary layer recovers in a very short distance before C_f reaches a peak value at 3%C_a, and the flow becomes fully turbulent.

In the 3D-cascade flow, C_f decreases between 3%C_a and 23%C_a due to the relaminarization, which is clearly identified by the contours of u'_t in Figure 16(a). Some weak streaks stretched in the stream-wise direction, which characterize the Klebanoff distortions, can be found in this region. Corresponding to this laminar region, C_p at the suction surface has a favorable pressure gradient from 3%C_a to 10%C_a, see Figure 4(b). C_f rises again at

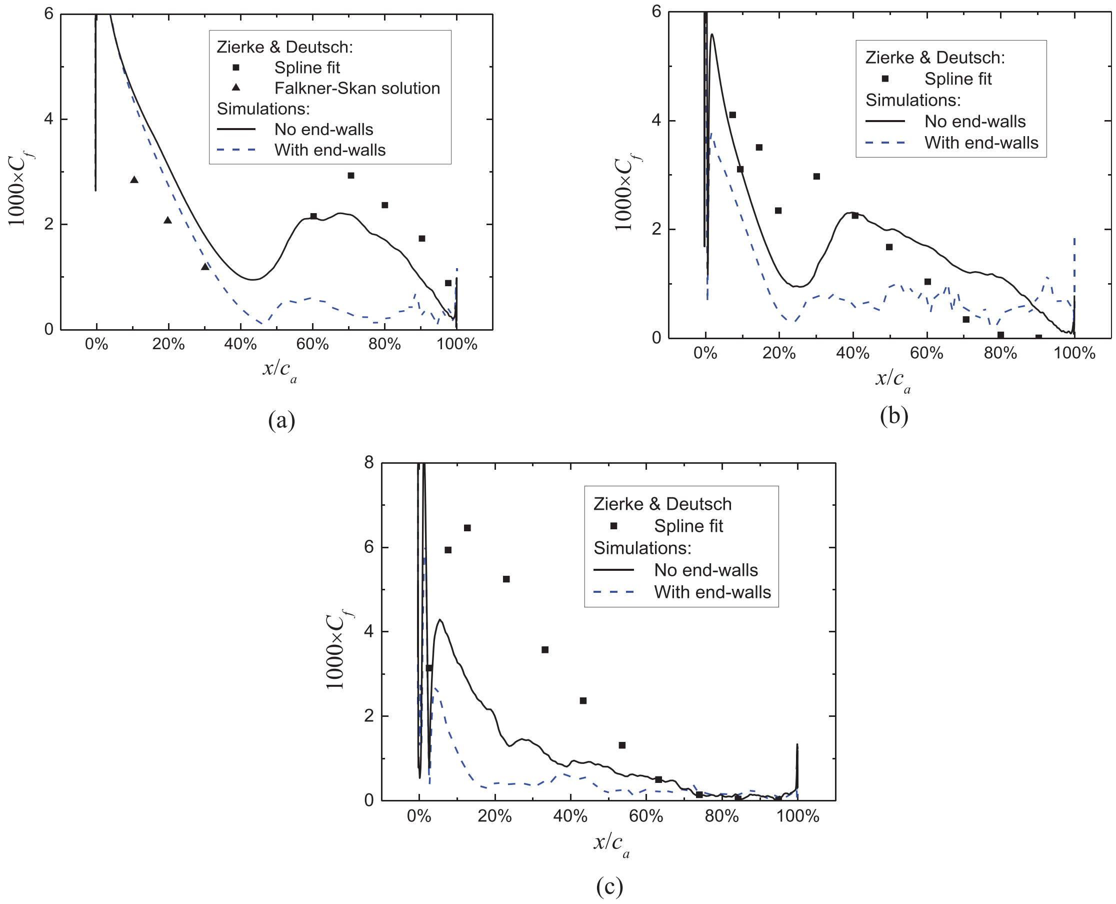

FIG 14. Friction coefficient over the suction surface for $\alpha = -8.5°$ (a), $-1.5°$ (b), and $5°$ (c).

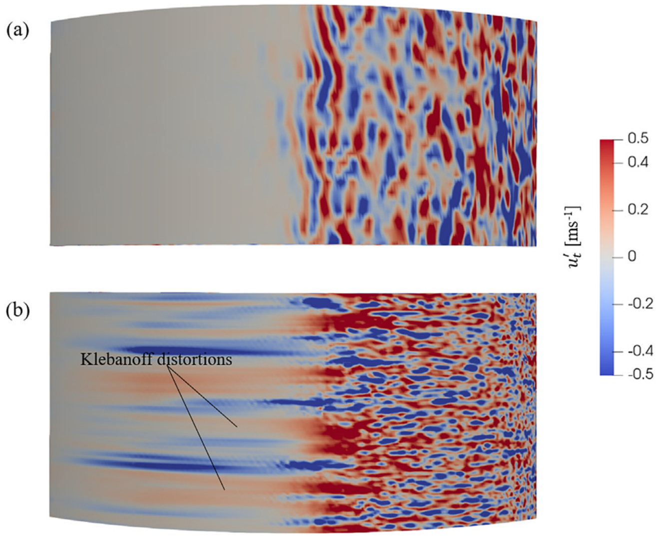

FIG 15. Contours of the instantaneous tangential velocity perturbation u_t' over the suction surface near the mid-span for $\alpha = -8.5°$. Results of the 3D-cascade flow (a) are compared with those of the 2D-cascade flow (b).

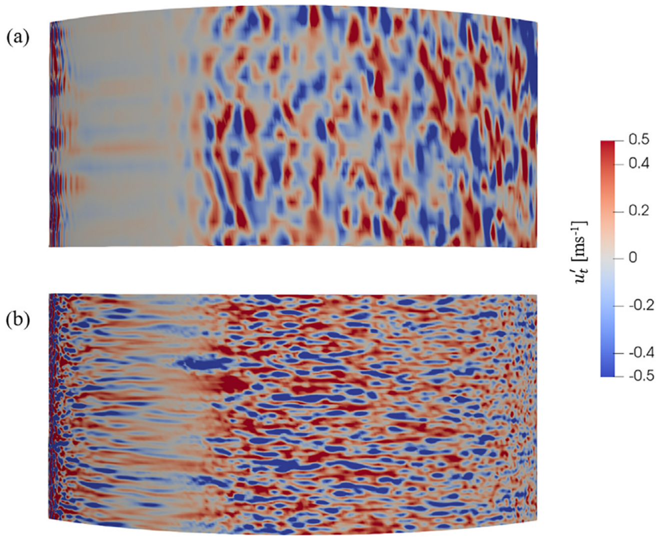

FIG 16. Contours of the instantaneous tangential velocity perturbation u_t' over the suction surface near the mid-span for $\alpha = -1.5°$. Results of the 3D-cascade flow (a) are compared with those of the 2D-cascade flow (b).

23%C_a due to the transition. Figure 16(a) shows that the span-wise elongated disturbances are dominant, so the transition still generally follows the mechanism of natural transition. The transition is completed at about 30%C_a, downstream of which the flows starts to separate.

Similar to the 3D-cascade flow, C_f also decreases between 3%C_a and 20%C_a in the 2D-cascade flow. However, the flow does not become laminar completely due to the strong stream-wise elongated perturbations. Figure 16(b) shows the stream-wise elongated streaks in this region evidently. C_f rises again at 25%C_a due to the transition to fully developed turbulence, then reaches another peak at 40%C_a, characterizing the starting point of flow separation. However, C_f does not completely vanish at the suction surface. This deviates from the experiment which suggests that C_f becomes zero downstream of 85.8%C_a.

Turbulence over the suction surface becomes stronger for $\alpha = 5°$. Two local minimum values of C_f are observed near the leading edge in the numerical results of both 2D- and 3D-cascade flows, see Figure 14(c), suggesting that two separation bubbles originate in this region. The boundary layer recovers in a short distance downstream of each bubble, indicated by a sharp rising of C_f. For the 3D-cascade flows, the turbulence becomes fully developed at 5%c_a, where C_f reaches a peak value. The flow starts to separate downstream of 5%c_a. The contours of u_t' show the disturbances elongated in the span-wise direction where the turbulence is fully developed, see Figure 17(a).

In the 2D-cascade flow, the turbulence becomes fully developed at about 8%c_a, indicated by a peak value of C_f in Figure 14(c). Downstream, stream-wise elongated disturbances dominate the flow, see Figure 17(b). Compared with the 3D-cascade flow, the boundary layer of the 2D-cascade flow recovers in a slightly longer distance. However, the predicted recovery distance is still shorter than the experiment, which suggests that the turbulence becomes fully developed at about 15%c_a. In addition, the experiment suggests that C_f reaches a higher peak value and decreases more slowly. C_f vanishes at about 81.5%c_a; this is close to the numerical results of the 2D-cascade flow. Again, this gap is expected to be due to the reason that the strong suction used in the experiment suppresses the development of turbulence. The numerical simulations still cannot represent the flow dynamics in the experiment near the suction surface for high incidence angles.

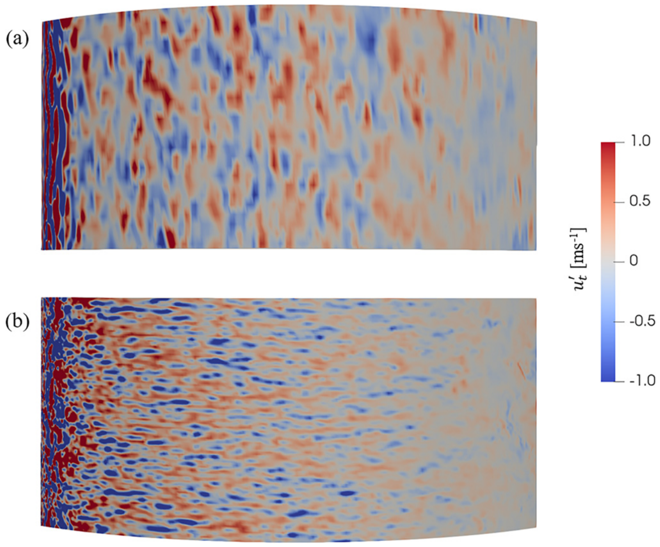

FIG 17. Contours of the instantaneous tangential velocity perturbation u_t' over the suction surface near the mid-span for $\alpha = 5°$. Results of the 3D-cascade flow (a) are compared with those of the 2D-cascade flow (b).

E. Wake

The iso-surfaces of Q colored by the span-wise velocity component u_3 in Figures 7 and 13 show the significant influences of the end-walls on the passage vortex. They cause the suction-side leg of the horse-shoe vortex to roll up toward the mid-span [Figure 13(a)] and the pressure-side leg of the horse-shoe vortex to fall down toward the end-walls [Figure 7(a)]. This strong span-wise disturbances can be still

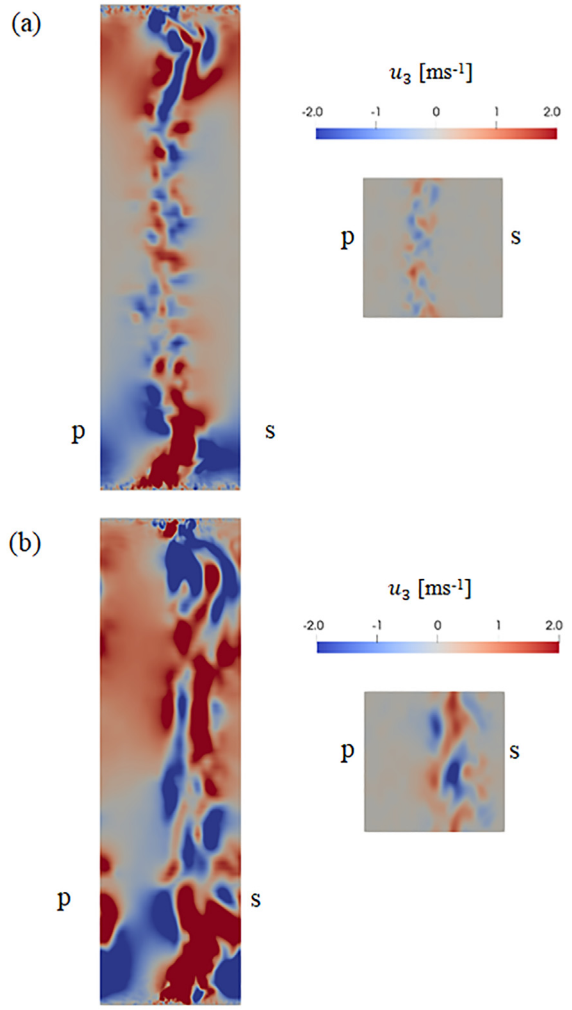

FIG 18. Instantaneous contours of the velocity component u_3 at the plane 31.9%c_a downstream of the trailing edge for $\alpha = -8.5°$ (a) and 5° (b). 3D-cascade flows (left side) are compared with 2D-cascade flows (right side).

felt in the wake. Figure 18 shows that, when the incidence angle is increased from $-8.5°$ to $5°$, the span-wise fluctuations in the wake are further enhanced and shifted away from the suction surface. Without accounting for the effect of end-walls, the span-wise fluctuations for $\alpha = 5°$ are considerably under-predicted, see Figure 18(b).

The distributions of the local total pressure loss coefficient ω_{xyz} at the plane 31.9%c_a downstream of the trailing edge are shown in Figure 19. The statistical results of the 3D-cascade flows are almost symmetric at the mid-span, suggesting that the span-width used in the simulation is long enough. However, the non-zero zone of ω_{xyz} for $\alpha = 5°$ is considerably thickened in the 3D-cascade flow. The reason is that, the end-walls lead to strong rolling-up of the flow, which induce strong fluctuations of the velocity near the mid-span. These fluctuations result in more loss of the kinetic energy; however, they are not correctly identified in the 2 D-cascade simulations. This explains why the simulations of 2D cascade flows over predict the pressure increase coefficient C_{p2} (Figure 5) and under-predict the total pressure loss coefficient ω (Figure 6) at large incidence angles.

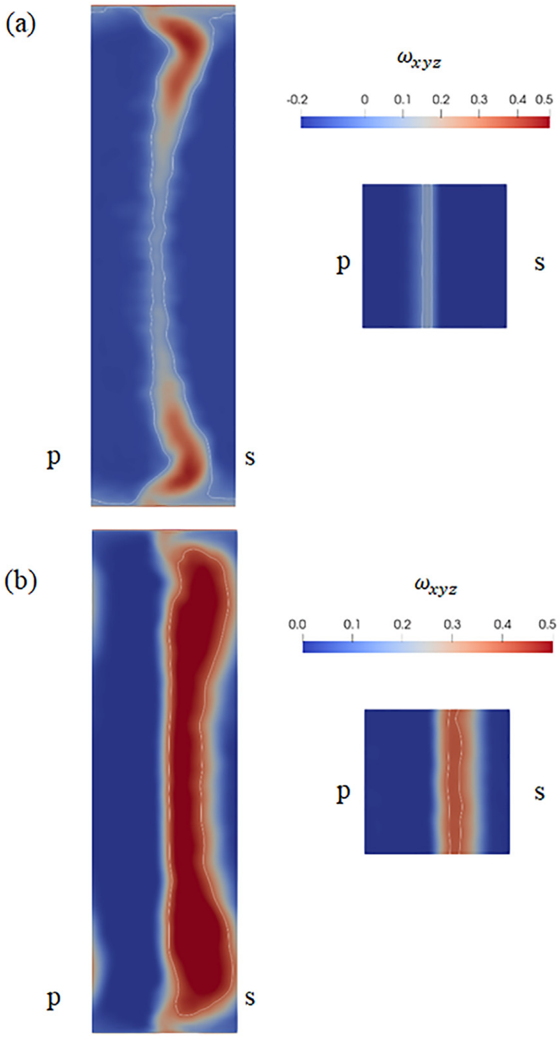

FIG 19. Local total pressure loss coefficient ω_{xyz} in the plane 31.9%c_a downstream of the trailing edge for $\alpha = -8.5°$ (a) and $5°$ (b). 3D-cascade flows (left side) is compared with 2D-cascade flows (right side).

The numerical results for the dimensionless mean stream-wise velocity υ are compared with the experimental data in Figure 20. υ is defined as

$$\upsilon = \frac{u_e - \overline{u}_1}{u_e - u_{cl}}, \tag{12}$$

where u_e is the mean streamwise velocity at the wake edge (approximated as the maximum streamwise velocity in the wake) and u_{cl} is the mean streamwise velocity at the wake centerline (approximated as the minimum streamwise velocity in the wake). As is expected, the wake becomes wider when the end-walls are accounted for, while the numerical results become closer to the experimental data. Although there is still a gap in the plane 52.6%c_a downstream of the trailing edge, the numerical results clearly indicate the necessity of considering the effects of end-walls for validating the numerical results with the experiment.

V. CONCLUSIONS

Since profound experimental data about flows in a highly loaded compressor cascade were published by Zierke and Deutsch in the late 1980s, very few numerical studies used these data to validate their numerical results. We have carried out a numerical study to better understand the flows in this cascade. A 2D-cascade (with periodic boundary conditions in both pitch-wise and span-wise directions) and a 3D-cascade (with a periodic boundary condition in the pitch-wise direction and two end-walls) are considered in the simulation.

For the incidence angle $\alpha = -8.5°$, the numerical results of the 2D-cascade flow, including the pressure coefficient C_p and friction coefficient C_f at the blade surfaces and the pressure increase coefficient C_{p2} and total pressure loss coefficient ω in the wake, are in an excellent accordance with the experimental data. This not only validates the numerical simulation but also shows that the experiment produces a 2D and periodic flow successfully by using a strong suction upstream of the blade leading edge. However, the simulations for $a = -1.5°$ and $5°$ over-predict C_{p2} and under-predict ω in the wake considerably. As a result, the calculated C_p at the blade surfaces also deviates from the experimental data. This discrepancy is expected to be due to the strong effects of the end-walls on the wake.

The flows in the 3D-cascade are simulated to further understand this problem. The numerical results confirm the strong effects of the end-walls on the wake. The end-walls induce span-wise elongated vortices and enhance the flow separation near the mid-span. The calculated C_p, C_{p2}, and ω for all three incidence angles are in good accordance with the experimental data. This shows the significance of considering the effects of end-walls for generating experimental data to validate numerical simulations. The calculated C_f deviates from the experimental data. This means that the predicted laminar-turbulent transition near the blade-surface is still different from the experiment. The reason is that a strong suction is adopted upstream of the blade leading edge in the experiment; however, it cannot be accounted for in the 3D-cascade simulations. This deficiency nevertheless does not affects the accuracy of the calculated C_p, C_{p2}, and ω significantly. These quantities are not very sensitive to the transition mechanism near the blade surfaces.

The laminar-turbulent transition is studied based on our numerical results. It is found that, for 2D-cascade flows with a low free-stream

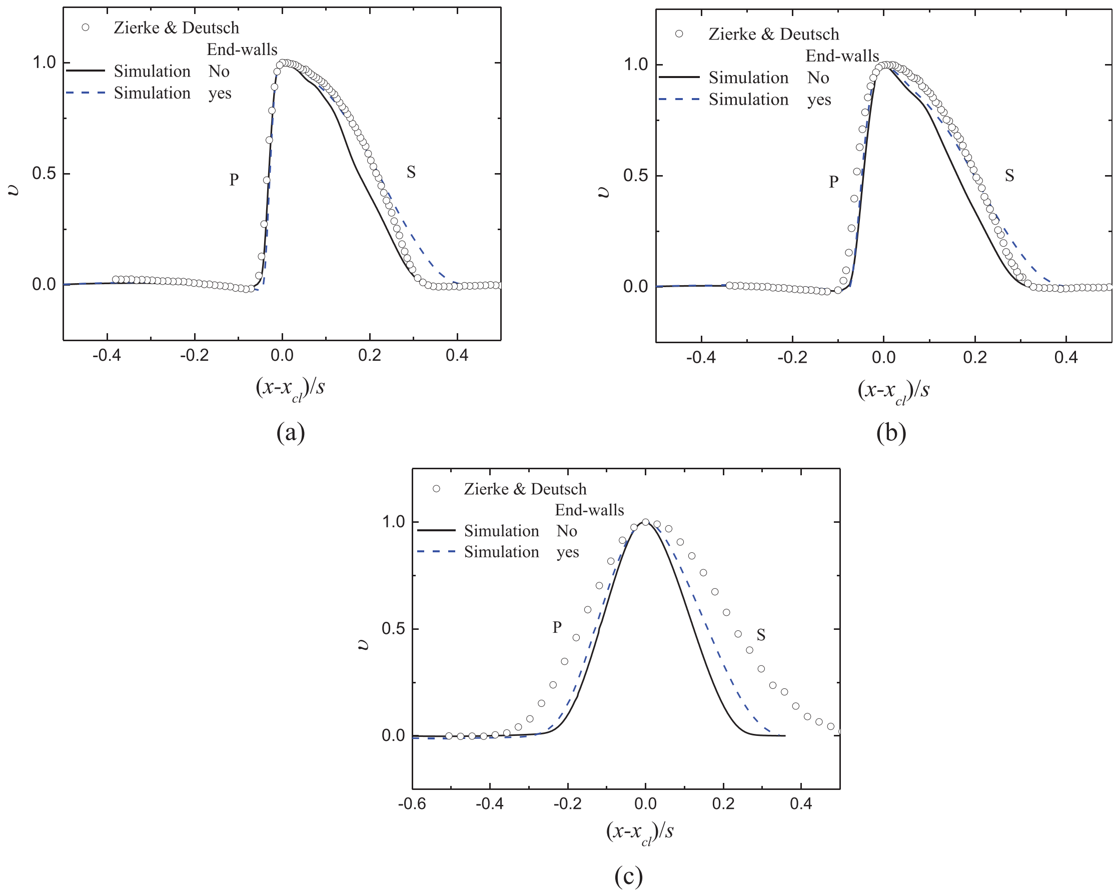

FIG 20. Dimensionless stream-wise velocity υ for $\alpha = 5^\circ$ in the plane 5.4%c_a (a), 9.6%c_a (b), and 52.6%c_a (c) downstream of the trailing edge.

turbulence intensity, the transition for $\alpha = 5^\circ$ on the pressure surface is determined by the interaction of the Klebanoff distortions and T–S waves. This is in accordance with the findings of Zaki *et al.*[11] Stream-wise elongated disturbances that characterize the Klebanoff distortions are also clearly identified on the suction surface for $\alpha = -8.5^\circ$.

For 3D-cascade flows, the elongated disturbances are considerably suppressed by the span-wise elongated disturbances, which are stimulated by the end-walls. These span-wise elongated disturbances dominate the transition for $\alpha = 5^\circ$ on the pressure surface and for $\alpha = -8.5^\circ$ on the suction surface. The transition for 3D-cascade flows generally follows the mechanism of natural transition.

ACKNOWLEDGMENTS

The authors gratefully acknowledge the support of this study by the DFG-Heisenberg program (299562371), the grant of the National Natural Science Foundation of China (No. 51922098). The calculations were carried out at the Computing Center of Hamburg University of Technology (RZ-TUHH) and the North-German Supercomputing Alliance (HLRN). Acknowledgement is also given to Mr. Es Sbai of University of Oldenburg for his contribution to the computational mesh.

AUTHOR DECLARATIONS

Conflict of Interest

The authors have no conflicts to disclose.

DATA AVAILABILITY

The data that support the findings of this study are available from the corresponding author upon reasonable request.

APPENDIX A: HIGH RESOLUTION RESULTS FOR THE 2D-CASCADE FLOW

Figure 21 shows the pressure coefficient C_p at the airfoil surface for $\alpha = 5^\circ$. The high mesh-resolution results are almost identical to the low mesh-resolution results. Both of them are higher than the experiment.

Figure 22 shows the instantaneous tangential velocity perturbations u_t' in a layer, which is 1.5×10^{-5} m away from the airfoil

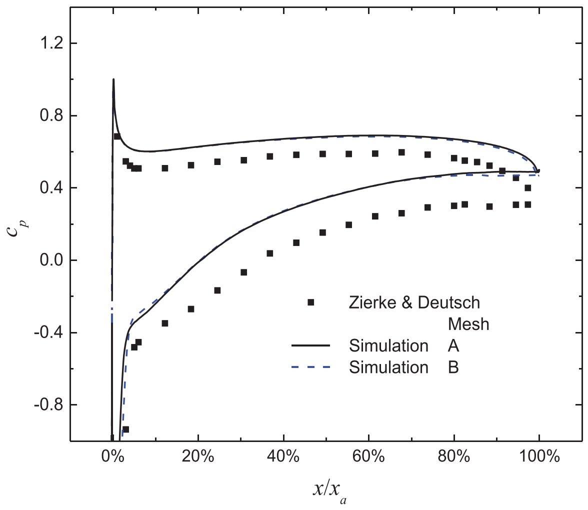

FIG 21. Pressure coefficient at the airfoil surface for $\alpha = 5°$. The results of the 2D-cascade flow are shown.

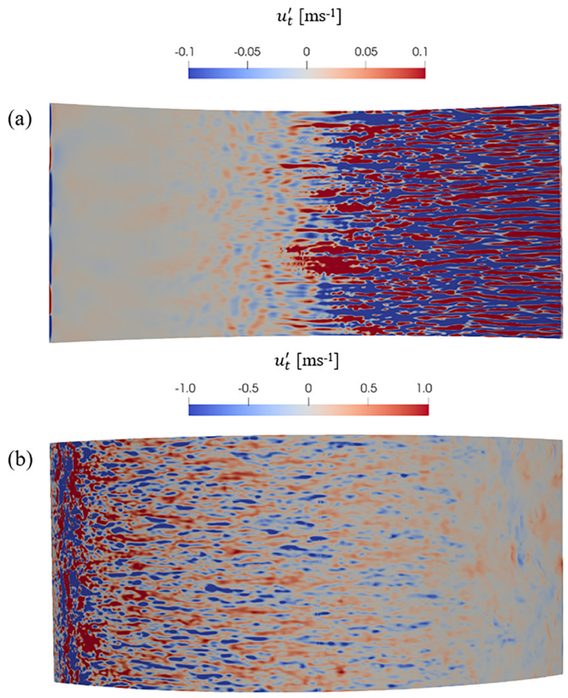

FIG 22. Contours of the instantaneous tangential velocity perturbations over the pressure surface (a) suction surface (b) near the mid-span for $\alpha = 5°$. The results of the 2D-cascade flow are shown.

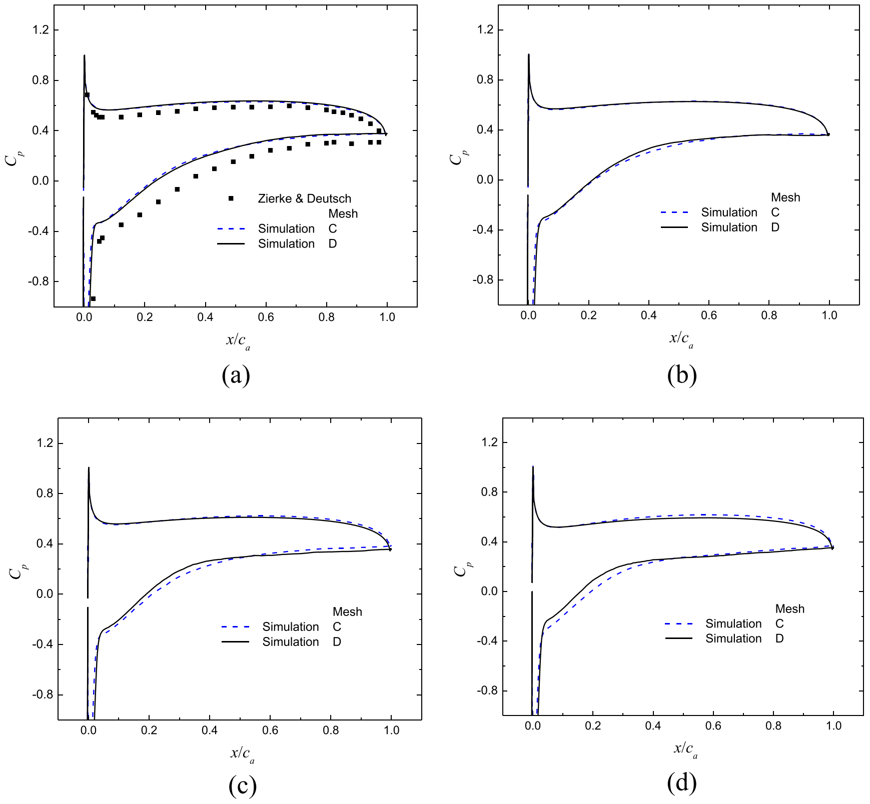

FIG 23. Pressure coefficient at the airfoil surface for $\alpha = 5°$ a t 50% (a), 30% (b), 20% (c), and 10% (d) span from an end wall. The results of the 3D-cascade flow are shown.

surface. The flow dynamics identified the contours of u_t' are also qualitatively similar to those indicated in the low mesh-resolution results, see Figures 11(b) and 16(b) for comparison.

APPENDIX B: HIGH RESOLUTION RESULTS FOR THE 3D-CASCADE FLOW

Figure 23 shows that, for the 3D-cascade flow with $\alpha = 5°$, the pressure coefficient C_p at the airfoil surface is slightly changed near the end wall when the number of mesh cells are increased by $3\times$. The flow near the mid-span, which is the focus of this study, is almost independent of the mesh resolution.

Figure 24 shows the instantaneous tangential velocity perturbations u_t' in a layer, which is 1.5×10^{-5} m away from the airfoil surface. The flow dynamics identified the contours of u_t' are also qualitatively similar to those indicated in the low mesh-resolution results, see Figures 11(a) and 17(a) for comparison. Some weak stream-wise elongated disturbances can be found over the suction surface; however, the span-wise elongated disturbances are still dominant.

Figure 25(a) shows that the vortices are sparsely populated over the pressure surface, suggesting that the turbulence is not fully developed. However, it is still possible to visualize a few λ-shaped vortices that originate from the viscous sub-layer. These λ-shaped vortices are more evidently identified by the contours of the instantaneous normal velocity perturbation u_n' [Figure 25(b)] in which the streaks of positive u_n' indicate that the vortices extrude from the viscous sublayer. The high mesh-resolution results suggest the same transition mechanism as the low mesh-resolution results. Therefore, the mesh resolution is sufficient for this study. However, simulations with a higher mesh-resolution are still needed to investigate more flow details near the blade surfaces quantitatively.

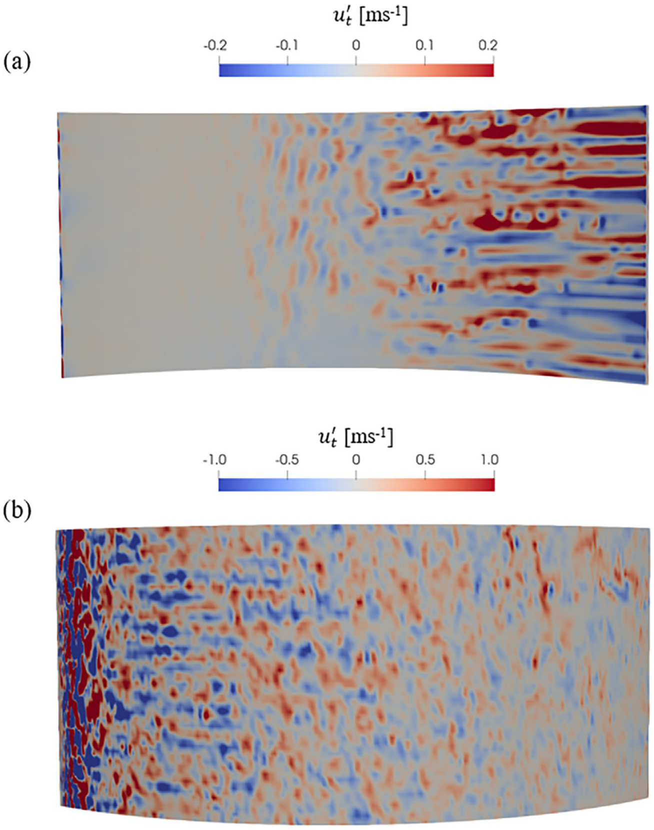

FIG 24. Contours of the instantaneous tangential velocity perturbations in the layer $y_w = 1.5 \times 10^{-5}$ m over the pressure surface (a) and suction surface (b) near the mid-span for $\alpha = 5°$. The results of the 3D-cascade flow are shown.

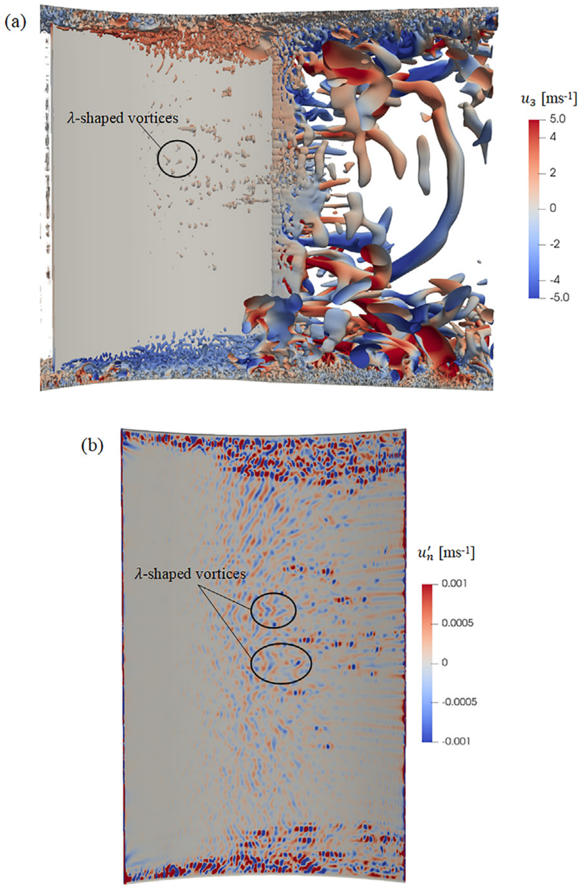

FIG 25. Vortical structures identified by $Qc^2/u_m^2 = 50$ colored with u_3 (a) and contours of the instantaneous normal velocity perturbation u_n' in the layer $y_w = 1.5 \times 10^{-5}$ m (b) over the pressure surface for the 3D-cascade flow with $\alpha = 5°$.

REFERENCES

[1] S. Deutsch and W. C. Zierke, "The measurement of boundary layers on a compressor blade in cascade at high positive incidence angle: Part II—data report," NASA Contractor Report 179492 (1986).

[2] S. Deutsch and W. C. Zierke, "The measurement of boundary layers on a compressor blade in cascade: Part 1—a unique experimental facility," ASME J. Turbomach. **109**, 520–526 (1987).

[3] S. Deutsch and W. C. Zierke, "The measurement of boundary layers on a compressor blade in cascade: Part 2—suction surface boundary layers," ASME J. Turbomach. **110**, 138–145 (1988).

[4] S. Deutsch and W. C. Zierke, "The measurement of boundary layers on a compressor blade in cascade: Part 3—pressure surface boundary layers and the near wake," ASME J. Turbomach. **110**, 146–152 (1988).

[5] W. C. Zierke and S. Deutsch, "The measurement of boundary layers on a compressor blade in cascade: Part 4—flow fields for incidence angles of −1.5 and −8.5 degrees," ASME J. Turbomach. **112**, 241–255 (1990).

[6] D. Vlahostergios, "Performance assessment of Reynolds stress and eddy viscosity models on a transitional DCA compressor blade," Aerospace **5**, 102 (2018).

[7] J. Du, Y. W. Li, Z. H. Li, J. C. Li, Z. N. Wang, and H. W. Zhang, "Performance enhancement of industrial high loaded gas compressor using Coanda jet flap," Energy **172**, 618–629 (2019).

[8] S. A. Gbadebo, N. A. Cumpsty, and T. P. Hynes, "Three-dimensional separations in axial compressors," ASME J. Turbomach. **127**, 331–339 (2005).

[9] V. M. Lei, Z. S. Spakovszky, and E. M. Greitzer, "A criterion for axial compressor hub-corner stall," ASME J. Turbomach. **130**, 031006 (2008).

[10] Y. Jin and H. Herwig, "Turbulent flow in rough wall channels: Validation of RANS models," Comp. Fluids **122**, 34–46 (2015).

[11] T. A. Zaki, J. G. Wissink, W. Rodi, and P. A. Durbin, "Direct numerical simulations of transition in a compressor cascade: The influence of free-stream turbulence," J. Fluid Mech. **665**, 57–98 (2010).

[12] X. Mao, T. A. Zaki, S. J. Sherwin, and H. M. Blackburn, "Transition induced by linear and nonlinear perturbation growth in flow past a compressor blade," J. Fluid Mech. **820**, 604–632 (2017).

[13] F. Gao, W. Ma, G. Zambonini, J. Boudet, X. Ottavy, L. Lu, and L. Shao, "Large-eddy simulation of 3-D corner separation in a linear compressor cascade," Phys. Fluids **27**, 085105 (2015).

[14] A. D. Scillitoe, P. G. Tucker, and P. Adami, "Numerical investigation of three dimensional separation in an axial flow compressor: The influence of free-stream turbulence intensity and endwall boundary layer state," J. Turbomach. **139**(2), 021011 (2017).

[15] B. Y. Min, J. Joo, J. Mendoza, J. Lee, G. P. Xia, and G. Medic, "Large-eddy simulation of corner separation in a compressor cascade," ASME Paper GT2018-77144 (2018).

[16] Z. Li, Y. P. Ju, and C. H. Zhang, "Parallel large eddy simulations of transitional flow in a compressor cascade with endwalls," Phys. Fluids **31**, 115104 (2019).

[17] Z. H. Li and R. K. Agarwal, "Investigation of endwall effect on transitional flow inside compressor cascade passage at low Reynolds number," Phys. Fluids **33**, 117108 (2021).

[18] H. Zhu, L. Zhou, and T. Meng, "Corner stall control in linear compressor cascade by blended blade and endwall technique based on large eddy simulation," Phys. Fluids **33**, 115124 (2021).

[19] M. Y. Wang, Z. L. Li, C. W. Yang, S. F. Zhao, Y. F. Zhang, and X. G. Lu, "Large eddy simulation of the separated flow transition on the suction surface of a high subsonic compressor airfoil," Phys. Fluids **32**, 034110 (2020).

[20] Z. N. Wang and X. Yuan, "Unsteady mechanisms of compressor corner separation over a range of incidences based on hybrid LES/RANS," ASME Turbo Expo 2013, GT2013-95300 (2013).

[21] J. F. Wu, "Improved delayed detached eddy simulation of compressor cascade tip leakage flow," Int. J. Aeronaut. Space Sci. **22**, 17–32 (2021).

[22] G. P. Xia, G. Medic, and T. J. Praisner, "Hybrid RANS/LES simulation of corner stall in a linear compressor cascade," ASME J. Turbomach. **140**, 081004 (2018).

[23] D. Lin, X. Yuan, and X. R. Su, "Local entropy generation in compressible flow through a high pressure turbine with delayed detached eddy simulation," Entropy **19**(1), 29 (2017).

[24] R. Y. Li, L. M. Gao, C. Ma, S. Y. Lin, and L. Zhao, "Corner separation dynamics in a high-speed compressor cascade based on detached-eddy simulation," Aerosp. Sci. Technol. **99**, 105730 (2020).

[25] Z. F. Yin and P. A. Durbin, "Detached eddy simulation of transition in turbomachinery: Linear compressor cascade," ASME J. Turbomach. **144**, 1–10 (2022).

[26] Y. Jin, "Parameter extension simulation of turbulent flows," Phys. Fluids **31**, 125102 (2019).

[27] Y. Jin, "Parameter extension simulation of turbulent flows in a compressor cascade with a high Reynolds number," in *Proceedings of ASME Turbo Expo 2020: Turbomachinery Technical Conference and Exposition, GT2020-14809* (2020).

[28] W. Ma, "Experimental investigation of corner stall in a linear compressor cascade," Ph.D. thesis (Ecole Centrale de Lyon, France, 2012).

[29] G. Zambonini, X. Ottavy, and J. Kriegseis, "Corner separation dynamics in a linear compressor cascade," ASME Paper, GT2016-56454 (2016).

[30] E. R. van Driest, "On turbulent flow near a wall," J. Aerosp. Sci. **23**, 1007–1011 (1956).

[31] Y. Jin and H. Herwig, "Parameter extension method (PEM): An asymptotic extension of numerical and experimental flow and heat transfer results to further values of the inherent parameters," Heat Mass Transf. **48**, 823–830 (2012).

[32] Y. Jin and A. V. Kuznetsov, "Turbulence modeling for flows in wall bounded porous media: An analysis based on direct numerical simulations," Phys. Fluids **29**, 045102 (2017).

[33] Y. Jin, M. F. Uth, A. V. Kuznetsov, and H. Herwig, "Numerical investigation of the possibility of macroscopic turbulence in porous media: a DNS study," J. Fluid Mech. **766**, 76–103 (2015).

[34] S. Gasow, Z. Lin, H. C. Zhang, A. V. Kuznetsov, M. Avila, and Y. Jin, "Effects of pore scale on the macroscopic properties of natural convection in porous media," J. Fluid Mech. **891**, A25 (2020).

[35] S. Gasow, A. V. Kuznetsov, M. Avila, and Y. Jin, "A macroscopic two-length-scale model for natural convection in porous media driven by a species-concentration gradient," J. Fluid Mech. **926**, A8 (2021).

[36] H. K. Versteeg and W. Malalasekera, *An Introduction to Computational Fluid Dynamics: The Finite Volume Method*, 2nd ed. (Pearson Education, 2007).

[37] R. Poletto, T. Craft, and A. Revell, "A new divergence free synthetic eddy method for the reproduction of inlet flow conditions for LES," Flow Turbul. Combust. **91**(3), 519–539 (2013).

[38] Z. H. Li, Y. Jin, J. Du, H. W. Zhang, and C. Q. Nie, "Physical mechanisms investigation of sharkskin-inspired compressor cascade based on large eddy simulations," J. Turbomach. **143**(6), 061005 (2021).

[39] V. M. Falkner and S. W. Skan, "Some approximate solutions of the boundary layer equations," Philos. Mag **12**(7), 865–896 (1931).